Tribology International 226 (2027) 112530

Contents lists available at ScienceDirect

Tribology International

journal homepage: www.elsevier.com/locate/triboint

Full length article

Load-based pressure profile matching for highly deformable fluid film bearings

Dave D. Sonneveld *, Ron A.J. van Ostayen

Department of Precision and Microsystems Engineering, Delft University of Technology, Mekelweg 2, 2628CD Delft, The Netherlands

ARTICLE INFO

Dataset link: 10.4121/3fb28ed6-f59e-4163-beaa-9960968f0a6c

Keywords:
Compliant hydrostatics
Elastohydrostatic lubrication
Highly deformable fluid film bearings
Pressure profile matching

ABSTRACT

Standard fluid film bearings are rigid and designed to operate with fixed surface geometries and curvatures. Introducing compliance in these bearings may extend their application range by allowing the bearing to adapt to wavy counter surfaces with a non-uniform curvature. As a result of this compliance, however, the film pressure might influence the bearing deformation. Despite existing solutions that have been proposed in literature, it remains a challenge to maintain a near-constant and efficient film profile under varying loads on functionally wavy surfaces. This work therefore presents a new design approach with a load-distributing support, based on the principle of pressure profile matching, to better control the deformability in these bearings. The fundamental working principle of this approach is shown and analyzed in a hydrostatic bearing. For this, an elasto-hydrostatic lubrication model is presented that combines the essential fluid-film and elastic behavior. The results show that, even with a limited number of distributed support forces, the approach maintains an improved performance on larger curvature variations. Based on these results, a practically usable range of the critical, non-dimensional design parameters is identified.

1. Introduction

The use of bearings is essential in machinery to reliably guide the motion between different parts. Among the common slider, roller and fluid film bearings, fluid film bearings are superior in terms of load capacity, wear and fatigue [1]. With their thin fluid film between the bearing and counter surface, they avoid direct contact and distribute the load over a large area. Yet their performance strongly depends on forming and maintaining the lubricating film, which is typically in the order of 100 μm thin. Because of this small fly height, even minor surface deformations can alter the film pressure and degrade the bearing performance. Classic designs of journal and thrust bearings therefore use stiff embodiments in which the bearing and counter surface are machined to the same curvature. The use of rigid embodiments, however, prevents these bearings from adapting their geometry to wavy or non-uniform surfaces. As a result, rollers are commonly used in applications with non-uniform curvatures.

A typical application with such curvatures is seen in cam-follower systems, where rollers move over a wavy cam profile to generate a desired motion in the followers as seen in Fig. 1. In contrast to surface irregularities or manufacturing deviations, the varying curvature of such a cam profile is an intentional part of the design, referred to as a 'functional wavy surface' in this work. These systems have been studied extensively in valvetrains of internal combustion engines [2–5], but large-scale applications have emerged. In particular, hydraulic drivetrains are developed for wind turbines to achieve a high power-to-weight ratio and an improved reliability [6–8]. For these drivetrains, large-scale radial piston pumps are investigated that incorporate many cam-roller interfaces [8–11]. At higher power ratings though, the loads on these interfaces increase substantially, as has been shown in a 600 kW example where the roller contacts proved to be critical [10]. Increasing the roller sizes to reduce contact stresses is not a straightforward solution in this case, as this adds inertia and thereby raises the risk of slippage between the roller and cam-surface [12,13]. Combined, these challenges motivate the development of highly deformable fluid film bearings as an alternative for high-load cam-roller applications, as schematically shown in Fig. 1. Here, 'high-load' refers to loads of 10–100+ kN [10], while 'highly deformable' refers to bearing deformations of 10–100 times the nominal film height [14].

The literature on deformable fluid film bearings, however, is rather limited. Early studies mainly focused on rubber supports, either as pivots to allow rigid pads to tilt and increase the load capacity [15,16], or as deformable pads for deformations in the order of the film height [17–20]. Other works only focused on compliant elements in parts of the bearing surface, to make the recess shape adaptable and thereby enhance the load capacity and film stiffness [21–23]. Alternatively, one study proposed a whiffletree-structure to support multiple

* Corresponding author.
E-mail address: d.d.sonneveld@tudelft.nl (D.D. Sonneveld).

https://doi.org/10.1016/j.triboint.2026.112530
Received 17 April 2026; Received in revised form 22 July 2026; Accepted 29 July 2026
Available online 3 August 2026

List of symbols

Latin

d	Vertical pad translation [m]
h	Film thickness [m]
t	Pad thickness [m]
u	Horizontal pad deformation [m]
w	Vertical pad deformation [m]
x	Horizontal coordinate [m]
z	Vertical coordinate [m]
A'_o	Orifice cross section per unit depth [m]
C_d	Orifice discharge coefficient [–]
E	Modulus of elasticity [Pa s]
F'	Bearing load per unit depth [N/m]
L	Bearing length [m]
N_x	Number of support forces [–]
P	Pressure [Pa]
Q'	Fluid flow per unit depth [m^2/s]
R	Radius of curvature [m]

Greek

α	Land width fraction [–]
β	Pressure ratio [–]
η	Dynamic visocity [Pa s]
$\bar{\kappa}$	Dimensionless surface curvature [–]
ν	Poisson ratio [–]
θ	Angle/rotation [rad]
ρ	Fluid density [kg/m^3]

Subscripts

f	film
m	mechanical support
min	minimum
n	nominal
p	pad
r	recess
s	supply
t	track

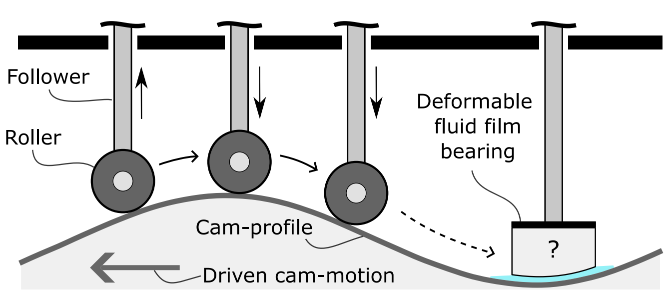

Fig. 1. Schematic example of a functional wavy surface in a cam-follower system, with the desired transition to using deformable fluid film bearings.

small hydrostatic pads [24]. This, however, reduces the load capacity as the gaps between the pads result in a less efficient use of the available bearing area to generate a load-carrying fluid film pressure.

More recently though, two studies focused on design principles for larger deformable hydrostatic bearings with a single pad. The first study introduced the term 'compliant-hydrostatic pre-loading' to describe the effect that compliant bearings could already deform by the film pressure when no adaptation of the bearing geometry is needed [14]. In standard geometries, such deformations negatively impact the film profile and pressure, decreasing the film stiffness and increasing the flow rate of the bearing [25]. So to minimize these side-effects, the study proposed the principle of 'pressure profile matching', which is further explained in the method of this paper. Using a stiffness-based approach of the principle, simulations showed that it can enable a bearing operation without undesired deformations on both a flat and sinusoidal surface with a 10 mm amplitude under a constant load [14]. For cam-follower systems, however, this approach contains two limitations. First, it is argued in this paper that the relative low bearing stiffness that is required for the stiffness-based approach [26] could impact the bearing performance under the varying loads that are typical in cam-follower systems. Second, the 10mm amplitude is still considered small, smaller than required, as the study used large bearing dimensions and a long wavelength compared to this amplitude. The second study therefore proposed a compliant, fluid-filled cell as a new deformable bearing concept [27]. A prototype of this concept was demonstrated to work at curvatures a 100 times larger (relative to bearing size) than the first study. The results, however, also revealed that it remains susceptible to compliant-hydrostatic pre-loading, which reduced the length of the thin fluid film to a relatively small edge near the perimeter of the bearing. As a result, the prototype operated with a six times higher flow rate than a rigid, recessed bearing embodiment.

Further research is thus necessary to control the deformations in highly deformable fluid film bearings and make them operate with an efficient film profile. A novel concept for a similar problem was recently presented to control the film height in the elasto-hydrodynamic process of roll-to-plate nano-imprinting [28]. Building on this work, the current paper aims to extend its application to hydrostatic bearings and larger functional curvatures, to control the film profile of deformable fluid film bearings under varying curvatures and loads. To do so, the classical design approaches and requirements from previous studies are discussed in a hydrostatic context, leading to a new load-based approach of the pressure profile matching principle. Next, the performance of the approach is analyzed by a two-dimensional (2D) implementation for a centrally fed hydrostatic bearing. Its numerical model is presented, followed by simulations of its behavior and an analysis on the influence of the design parameters. Accordingly, design rules for largely deformable hydrostatic bearings are given and the generalization of the approach to other fluid film bearings is discussed.

2. Method

This section first introduces the fundamental concept. Next, the governing equations of this concept are presented for a hydrostatic example, followed by its numerical implementation.

2.1. Concept

The central challenge in deformable fluid film bearings is that the film pressure and bearing deformation influence each other. Because of this coupling, highly deformable fluid film bearings must be designed differently than rigid bearings. To motivate this and to introduce the load-based approach, the classical design approaches are first discussed in a 2D context.

2.1.1. Classical design approaches

A schematic of the classical bearing approaches and the load-based approach is shown in Fig. 2. In rigid bearings, the shape of the bearing surface, and thus the lubricating film profile in a nominal condition, are fully defined by the design. Different shapes can be selected to obtain different height and pressure profiles, like a recessed film with a trapezoidal pressure as seen in Fig. 2(a). By 'nominal', this paper refers to a representative operating condition, defined by the load, fly-height and surface curvature. Here, the nominal surface shape is

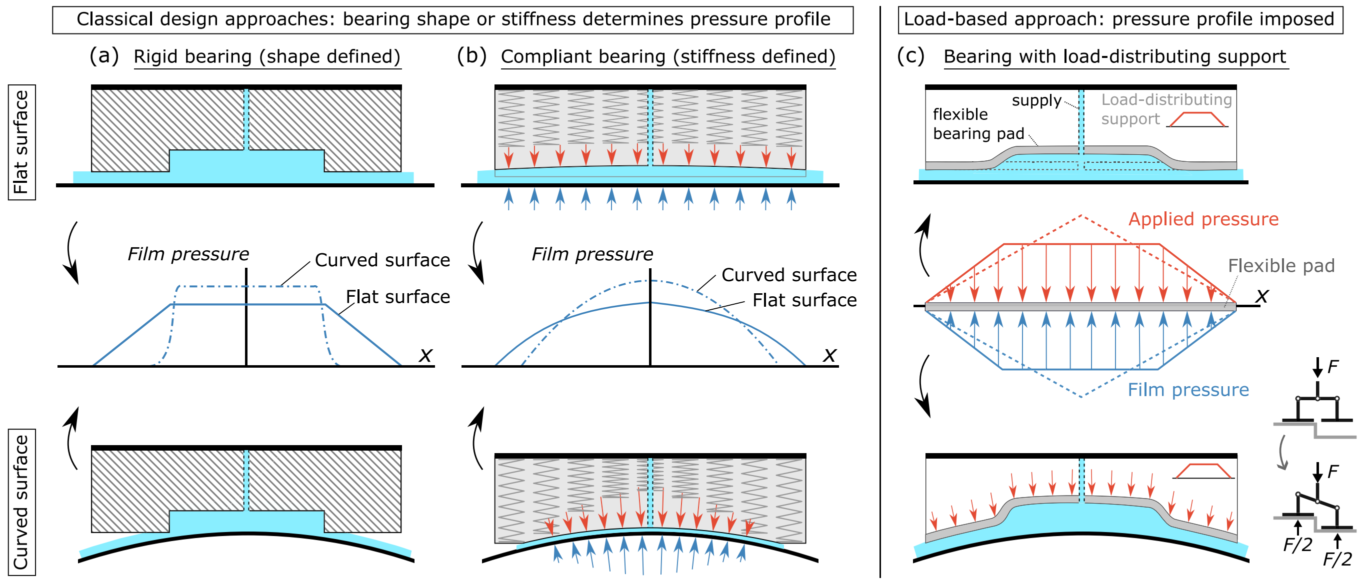

Fig. 2. Schematics of different (hydrostatic) design approaches for fluid film bearings, showing their behavior on a flat and curved surface. (a) Rigid bearings where the pre-defined geometry determines the pressure profile. Here, the bearing is designed for a flat surface. (b) Standard compliant bearings where the film pressure adapts to the support pressure (red arrows pointing downwards), which is related to the bearing deformation. (c) The new load-based approach for pressure profile matching, which applies the desired pressure profile to a flexible bearing pad. Accordingly, the pad adapts relative to the surface until the fluid film matches the applied pressure. To apply the load, a zero-stiffness load-distributing support is assumed, which distributes the load normal to the pad independent of its shape.

defined to be flat, as this represents the average curvature in many wavy surfaces [14]. Once the load deviates from the nominal condition, a rigid bearing will adapt its global orientation to form a different film and pressure profile that support the new load-condition. Yet on different surfaces shapes, as seen in the bottom of Fig. 2(a), they quickly lose the intended film height and pressure profile.

In compliant bearings, the pressure profile also depends on the deformation of the bearing surface and its influence on the film profile. To illustrate this, a basic rubber bearing design is considered in Fig. 2(b). Here, the compliancy is represented by the vertical compression springs. To obtain an equilibrium with the fluid film, the contact pressure of the bearing surface (i.e. the compressive forces from the springs) should match the fluid film pressure. On the nominally flat surface, this explains the previously mentioned effect of compliant-hydrostatic pre-loading: the film pressure compresses the springs and the resulting deformation affects the film pressure. On more curved surfaces though, the bearing deformation starts to dominate this equilibrium, similar to the effect in strongly deformed and lubricated contacts like rubber seals [29,30]. As the film thickness becomes negligible compared to the surface curvature, the macro-deformation of the bearing to form a thin fluid film (i.e. the global deformation of 10–100 times the film height to match the surface curvature) fully depends on the surface shape, as shown in Fig. 2(b). Based on the bearing stiffness, this macro-deformation prescribes the contact pressure to which the film pressure must adapt, which is possible by negligible micro-deformations (i.e. not larger than the order of the film height). In this way, the film pressure thus depends on the bearing's reaction to its macro-deformation, which can vary on different curvatures and thereby influence the film height, flow and overall performance that are coupled to the film pressure.

2.1.2. *Stiffness-based pressure profile matching*

The idea of 'pressure profile matching' is therefore to design the bearing's reaction profile such that it matches and induces the desired film pressure. The stiffness-based approach realized this with spatially varying stiffnesses in a design like Fig. 2(b) [14], as further detailed in Fig. 3. With low spring stiffnesses and a pre-compression that is significantly larger than the working deformations, these springs

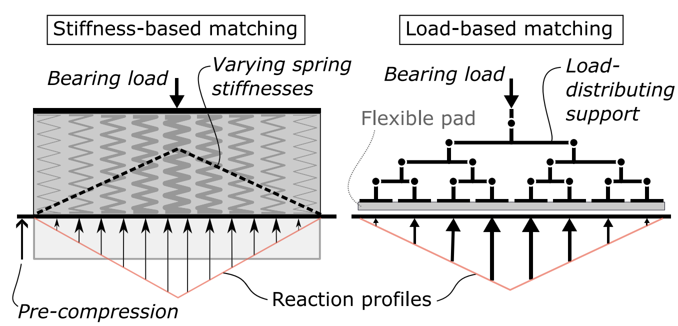

Fig. 3. Schematics of the stiffness-based approach and load-based approach for pressure profile matching to obtain a specific reaction profile of the support.

can maintain a close to constant reaction profile on varying curvatures [26]. The dependency on a pre-compression and low spring stiffnesses, however, poses two limitations. In applications with variable loads, such as in cam-follower systems [12], a low stiffness leads to changing compressions that affect the tracking performance. In addition to this, the pre-compression becomes strongly load-dependent with low spring stiffnesses. Hence, lower loads can reduce the pre-compression and thereby the invariance of the bearing's reaction profile to its deformation.

2.1.3. *Load-based pressure profile matching*

To avoid the pre-compression and low spring stiffnesses, this study proposes an alternative, load-based approach for pressure profile matching, based on a novel concept for a nano-scale imprinting process [28]. Instead of indirectly shaping the bearing's reaction profile by tuning the bearing stiffness and relying on its deformation, it focuses on applying the desired pressure profile directly to the film. Illustrated in Fig. 2(c), it is based on two key elements. The first element is a flexible bearing pad, which provides a continuous bearing surface and serves as the interface between the bearing support and the fluid film.

Ideally, this pad approaches a negligible bending stiffness, allowing it to deform under any pressure differences between the applied load and the fluid film until they become equal. Eventually, this should conform the pad to the bearing shape that corresponds to the applied load, as shown in the top of Fig. 2(c). The second element is a load-distributing support, which distributes the load in the desired pressure profile to the pad. If this load distribution operates normal to the pad's surface, independent of its shape as shown in the bottom of Fig. 2(c), the conforming ability should extend to curved surfaces and realize a constant bearing performance on varying surface shapes.

The load-based approach thus fundamentally differs from the stiffness-based approach in how it realizes the desired pressure distribution. It focuses on directly distributing the bearing load in the desired pressure profile to the pad, instead of using the deformation-dependent reaction profile of a compliant support. Yet to achieve the load distribution passively at variable loads, the support must satisfy two stiffness conditions [27]. Ideally, the support should exhibit a low deformation stiffness so it can passively adapt its shape by the first minimal changes in film pressure when a variation in surface curvature is experienced. Simultaneously, a high compression stiffness is desired to support high loads and prevent varying compressions as mentioned with the stiffness-based approach. Hence, a stiffness trade-off can exist. In rubber bearings that mainly use compressions, as shown in Fig. 2(b), this trade-off is clearly present: low spring stiffnesses improve the adaptability, but increase compressions under varying loads. Avoiding the trade-off is possible though, by decoupling the deformation modes of the competing stiffnesses. A practical solution for this is found in underactuated differential mechanisms, of which a small example is shown in the bottom right of Fig. 2(c). By a rotation of the hinges, such a mechanism can freely adapt its shape until it settles on a surface. Once it is settled, it becomes stiff in compression as the rigid parts can no longer rotate and start to carry the load. Depending on the moment balance in the mechanism, the load is distributed in a specific profile to the surface, or the flexible pad in this study's application as shown in the right of Fig. 3. Any changes in the fluid film pressure likewise deform the load-distributing support until the moment balance is restored.

In reality, however, the ideal approach faces several practical limitations. The load distribution will likely be realized by a limited, discrete set of forces on the pad, which in turn requires a certain stiffness in the pad to maintain a smooth bearing surface between the applied forces. So, to prove the feasibility of the load-based approach, the remainder of this work focuses on modeling its fundamental working principle and analyzing the influence of these limitations. For this, a model is introduced that describes the behavior of the flexible pad, assuming that a perfect discretized load profile is distributed to its surface.

2.2. Elastohydrostatic model description

A representation of the bearing model for the flexible pad is shown in Fig. 4(a). For the fundamental pad behavior, the model considers a 2D implementation of the load-based approach in a centrally fed hydrostatic bearing. In this application, a flexible pad with length L and thickness t floats on a thin fluid film of thickness h, centered at $x = 0$. The distributed support load P_m is applied on top of the pad and assumed to act normal to the pad's surface. Its profile is defined by a trapezium shape with a mechanical land width fraction α_m, to approach both recessed ($\alpha_m < 0.5$) and zero recess ($\alpha_m \approx 0.5$) pressure profiles. The counter surface is fixed at the origin $(x, z) = (0, 0)$ and is nominally flat, from which it adapts to circular profiles with decreasing radii of curvature R_t to analyze the bearing's adaptation. In line with [27], this circular assumption is considered to be suitable for bearings that cover only a segment of wavy surfaces and is useful to obtain a single-parameter surface metric. Accordingly, the surface profile is given by

$$z_t = R_t - R_t \cdot \sqrt{1 - \left(\frac{x}{R_t}\right)^2}, \tag{1}$$

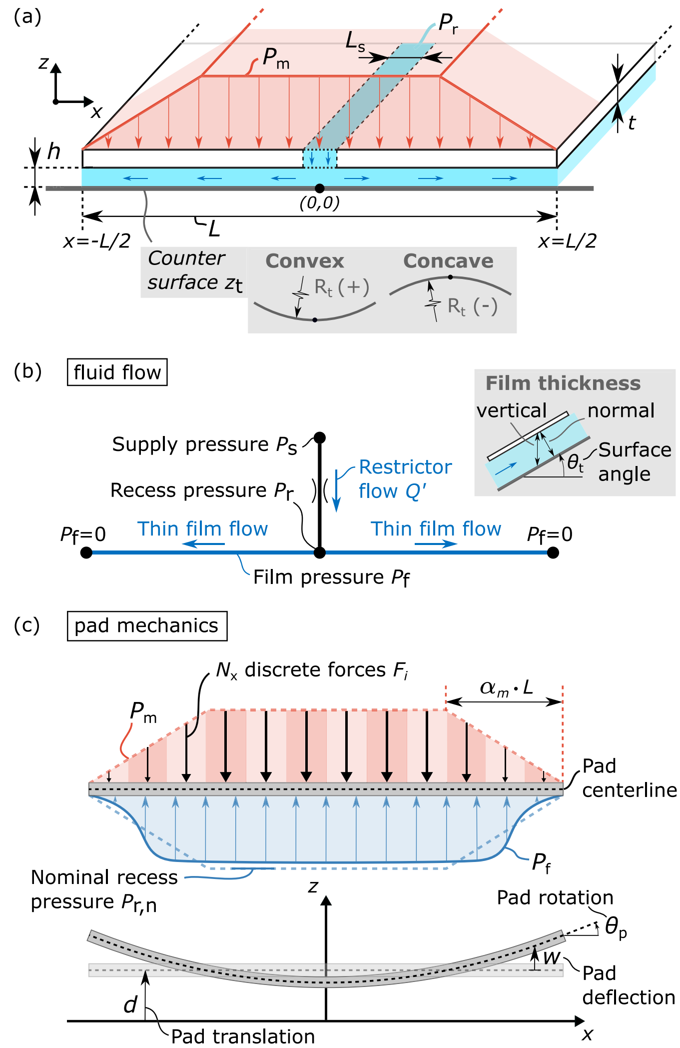

Fig. 4. Schematics of (a) the modeled 2D hydrostatic bearing system with the distributed applied load P_m, (b) the flow scheme of the bearing and (c) the pad deformation with the applied loads, including the discrete set of forces N_x.

where z_t is the surface height at coordinate x and the sign of R_t determines the surface direction. The fluid film is supplied by a fixed orifice restrictor and supply pressure P_s.

The model itself is governed by four main equations, grouped into two parts. The first part, describing the fluid flow as seen in Fig. 4(b), consists of a restrictor equation for the fluid supply and the Reynolds equation for the flow in the film. The second part, describing the pad's deformation as seen in Fig. 4(c), consists of a load balance for the total load capacity and a moment–curvature equation for the bending of the pad. Together, these equations are solved simultaneously to determine the fluid film pressure P_f and the film thickness h, which depends on the pad's vertical rigid-body translation d and deflection w. In the formulations, these and other variables are scaled to ensure numerical robustness and to obtain a general, non-dimensional model. Using a bar over dimensionless quantities, this scaling is defined as

$$\bar{x} = \frac{x}{L}, \quad \bar{z} = \frac{z}{L}, \quad \bar{w} = \frac{w}{L}, \\ \bar{h} = \frac{h}{h_n}, \quad \bar{d} = \frac{d}{h_n}, \quad \bar{P} = \frac{PL}{F_n'}, \tag{2}$$

where the coordinates $(\bar{x}, \bar{z})$ and deformation $\bar{w}$ are scaled by the pad's length L, the film height $\bar{h}$ and translation $\bar{d}$ by the nominal film height

h_n, and the pressures $\bar{P}$ by the average pressure to sustain the nominal load capacity per unit depth F'_n. Based on this scaling, the equations are presented below.

2.2.1. Fluid flow

The flow through the restrictor and in the film is described by standard lubrication theory, using a restrictor relation for the supply flow and the Reynolds equation for the pressure distribution in the film. To focus on the interaction between the fluid film and the bearing, independent of specific fluid properties, Newtonian, isothermal, and incompressible flow conditions are assumed. In addition, a constant pressure across the film thickness and a steady-state operation are considered.

Under these assumptions, the Reynolds equation governing the film pressure $\bar{P}_f$ is given by [31] as

$$\frac{1}{L}\frac{\partial}{\partial \bar{x}}\left(-\frac{h_n^3 F'_n}{12\eta L^2}\bar{h}^3\frac{\partial \bar{P}_f}{\partial \bar{x}}\right) + \frac{1}{L}\frac{\partial}{\partial \bar{z}}\left(-\frac{h_n^3 F'_n}{12\eta L^2}\bar{h}^3\frac{\partial \bar{P}_f}{\partial \bar{z}}\right) = 0, \tag{3}$$

where η denotes the dynamic viscosity. The additional z-term here, compared to standard one-dimensional flow formulations, is used to model the fluid flow correctly in the spatial frame when the flow obtains a significant incline on circular surfaces. A zero-pressure boundary condition is further imposed at the pad's edges and the film thickness $\bar{h}$ is defined as

$$\bar{h} = \left(\bar{d} + \frac{L}{h_n}\bar{w} - \frac{L}{h_n}\bar{z}_t\right)\cdot\cos\theta_t. \tag{4}$$

Here, the terms within brackets represent only the vertical gap between the pad and the surface. For inclined flows, this does not correspond to the actual film thickness, as shown in Fig. 4(b). Hence, a cosine correction with the local surface angle θ_t is applied to approximate the normal film thickness. Due to the thin film this approximation is considered acceptable.

The supply flow through the orifice restrictor, which is implemented as a source term in Section 2.3, is given by [1] as

$$Q' = C_d A'_o \sqrt{\frac{F'_n}{L}}\sqrt{\frac{2(\bar{P}_s - \bar{P}_r)}{\rho}}, \tag{5}$$

where Q' is the flow per unit depth, C_d the discharge coefficient, A'_o the cross-sectional area per unit depth of the restrictor, ρ the fluid density and $\bar{P}_r$ the recess pressure. In rigid bearings with a pre-defined film and pressure profile (see Fig. 2(a)), the design parameters $\bar{P}_s$ and A'_o are typically chosen to achieve a desired nominal load and fly height. For the deformable bearing pad, the same approach is applied by assuming that the pad adapts by any initial pressure differences between the film pressure and the distributed load P_m, such that its film geometry and pressure eventually match with P_m as in Fig. 2(c). In this way, $\bar{P}_s$ and A'_o can be expressed in terms of the nominal condition of P_m.

For $\bar{P}_s$, the nominal pressure profile is first described in terms of the nominal load capacity. Integrating the trapezium pressure profile over the pad's length, the dimensionless nominal recess pressure $\bar{P}_{r,n}$, indicated in Fig. 4(c), should be equal to

$$\bar{P}_{r,n} = \frac{1}{1-\alpha_m}. \tag{6}$$

Depending on the desired pressure ratio $\beta = \bar{P}_{r,n}/\bar{P}_s$, the dimensionless supply pressure then follows as

$$\bar{P}_s = \frac{1}{\beta(1-\alpha_m)}. \tag{7}$$

In order to determine the cross sectional area of the restrictor A'_o, the flow is considered around the supply region. With a predominantly horizontal flow at the origin, the division of the supply flow into the left and right parts of the fluid film can be described with the first flow term in brackets in Eq. (3) by

$$Q' = \frac{h_n^3 F'_n}{12\eta L^2}\left(-\left(\bar{h}^3\frac{\partial \bar{P}_f}{\partial \bar{x}}\right)_{\text{left}} - \left(\bar{h}^3\frac{\partial \bar{P}_f}{\partial \bar{x}}\right)_{\text{right}}\right). \tag{8}$$

In the nominal condition, the flow equally divides to both sides of the film. Based on a nominal film thickness at the land width area and the linear pressure drop in the trapezium profile in this same region, Eq. (8) can describe the nominal condition by

$$C_d A'_o \sqrt{\frac{F'_n}{L}}\sqrt{\frac{2(\bar{P}_s - \bar{P}_{r,n})}{\rho}} = 2\cdot\frac{h_n^3 F'_n}{12\eta L^2}\frac{1}{\alpha_m(1-\alpha_m)}, \tag{9}$$

where Q' is based on the nominal recess pressure. Substituting the pressures from Eqs. (6) and (7), A'_o can be expressed as

$$A'_0 = \frac{h_n^3}{6\eta C_d}\frac{\sqrt{\rho F'_n}}{L\sqrt{2L}}\frac{1}{\alpha_m\sqrt{(1-\alpha_m)(\frac{1}{\beta}-1)}}. \tag{10}$$

To simplify the system of equations, the expression for A'_o is substituted in Eq. (5). For this, it is assumed that the discharge coefficient C_d is constant, based on a high Reynolds number in the supply flow as is common for orifice-compensated hydrostatic bearings [1,31]. After rewriting, Eq. (8) then becomes

$$\frac{2\sqrt{\bar{P}_s - \bar{P}_r}}{\alpha_m\sqrt{(1-\alpha_m)(\frac{1}{\beta}-1)}} = -\left(\bar{h}^3\frac{\partial \bar{P}_f}{\partial \bar{x}}\right)_{\text{left}} - \left(\bar{h}^3\frac{\partial \bar{P}_f}{\partial \bar{x}}\right)_{\text{right}}, \tag{11}$$

where the left hand side represents the simplified restrictor flow Q'. Accordingly, the Reynolds equation is simplified to

$$\frac{\partial}{\partial \bar{x}}\left(-\bar{h}^3\frac{\partial \bar{P}_f}{\partial \bar{x}}\right) + \frac{\partial}{\partial \bar{z}}\left(-\bar{h}^3\frac{\partial \bar{P}_f}{\partial \bar{z}}\right) = 0. \tag{12}$$

2.2.2. Pad mechanics

The deformations of the pad are modeled by considering the pad as a slender beam. Here, only bending is of interest under the assumption that the load-distributing support always acts perpendicular to the pad's surface, like the film pressure. Thus, the Euler–Bernoulli equation for pure bending of an infinitely wide beam is used to determine the deflection $\bar{w}$ by

$$\frac{\partial^2}{\partial \bar{x}^2}\left(\frac{Et^3}{12(1-\nu^2)F'_n L^2}\frac{\partial^2 \bar{w}}{\partial \bar{x}^2}\right) = \bar{P}_f - \bar{P}_m, \tag{13}$$

where E is the pad's modulus of elasticity, ν the Poisson ratio and $\bar{P}_m$ the distributed applied load from the support. In this study, $\bar{P}_m$ is represented by N_x discrete forces that are uniformly distributed over the pad's length, as illustrated in Fig. 4(c). Each force acts in the center of a pad-section with length L/N_x and an initial load $\bar{F}'_{i,n}$ that represents the pressure contribution above that element, as detailed further in Section 2.3. The boundary conditions of the pad are free on both ends, represented by

$$\left.\frac{\partial^2 \bar{w}}{\partial \bar{x}^2}\right|_{\bar{x}=\pm\frac{1}{2}} = 0, \qquad \left.\frac{\partial^3 \bar{w}}{\partial \bar{x}^3}\right|_{\bar{x}=\pm\frac{1}{2}} = 0. \tag{14}$$

For the balance between the applied load F' per unit depth, (distributed over N_x forces) and the fluid film, a summation over the forces and an integral over the film pressure are used as

$$\frac{F'}{F'_n} = \sum_{i=1}^{N_x}\bar{F}_i\cos(\theta_{p,i}), \tag{15}$$

$$\frac{F'}{F'_n} = \int_{\bar{x}=-\frac{1}{2}}^{\bar{x}=\frac{1}{2}}\bar{P}_f\cos(\theta_p)\,d\bar{x}, \tag{16}$$

where $\theta_p = \arctan(d\bar{w}/d\bar{x})$ represents the dimensionless angle of the pad. Based on Eq. (15), the initial values $\bar{F}_i$ can be scaled uniformly to match varying loads of F', thereby modeling the load-distributing function of the support. Likewise can Eq. (16) be evaluated to adapt the pad translation $\bar{d}$ until the film pressure matches the load capacity F' as well. The cosine terms in both equations ensure that only the vertical contribution of each load is evaluated at larger inclines of the pad.

Combining all equations, the deformation of the pad and its interaction with the fluid film are fully described. Based on the scaling

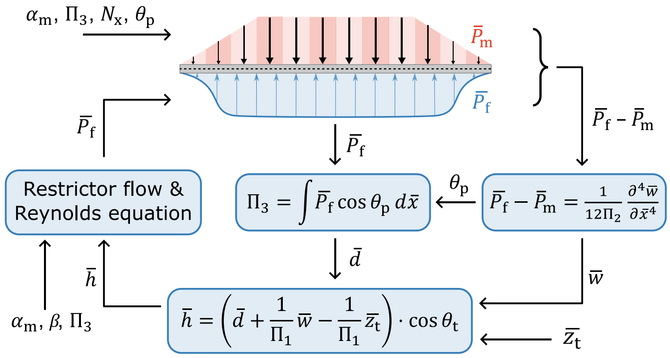

Fig. 5. Overview of the governing equations in the model, the relation of the variables between them and the implementation of the parameter groups Π_{1-3}.

in Eq. (2), three parameter groups emerge that reduce the number of independent input parameters. These are

$$\Pi_1 = \frac{h_n}{L}, \qquad \Pi_2 = \frac{F_n' L^2 (1-\nu^2)}{E t^3}, \qquad \Pi_3 = \frac{F'}{F_n'}, \tag{17}$$

where Π_1 represents the nominal film thickness compared to the bearing length, Π_2 the relative compliance of the pad in relation to the nominal load, and Π_3 the active load-ratio relative to the nominal load. Together with the land width α_m, pressure ratio β and the number of discrete forces N_x, these groups form the input parameters. An overview of their implementation and the relation between the equations in the model is given in Fig. 5.

2.3. Numerical implementation

The equations have been implemented in the finite element method (FEM) software of COMSOL Multiphysics [32]. Here, the unit system is set to "none" to obtain a unit-less model for the non-dimensional formulations. Accordingly, the equations can be implemented directly in their non-dimensional form as presented in the previous section, using the variables from Eq. (2) and the parameters Π_{1-3}, α_m, β and N_x as inputs.

The model itself is built in the 2D environment, in which the flexible pad is modeled as an Euler–Bernoulli beam according to Eq. (13). Physically, this equation represents the deformation of an infinitely wide pad and therefore corresponds to a plane-strain assumption. However, rather than using a 2D continuum where plane strain or stress needs to be selected, the behavior of the pad is implemented through COMSOL's Beam interface on a one-dimensional line domain, for computational efficiency. On the same line, the fluid flow is modeled mathematically by the Reynolds equation, using the General Form Boundary PDE (Partial Differential Equation) interface. The coupling between the interfaces is implemented manually through the governing equations, as explained at the respective interfaces below.

The geometry thus consists of a single, horizontal line that represents the flexible pad. Additionally, N_x points are placed on the line to apply the discrete support forces. The placement of these points is determined by equally dividing the line into N_x segments and placing a point in the center of each segment. For the numerical study, the line is meshed into 100 elements, of cubic order for both the beam and pressure elements, which was verified to be mesh converged in a separate study where no significant changes in the results were observed with further mesh refinements. Regarding the material of the pad, a standard linear elastic material is assigned to the line, defined by a Young's modulus of 1 and a Poisson's ratio of 0.49, which do not update with deformation. In fact, these parameters remain constant throughout the study, as the pad compliance is varied through the non-dimensional parameter group Π_2.

In the PDE interface, the Reynolds equation from Eq. (12) is implemented as a General Form Boundary PDE over the entire line domain, by setting the conservative flux Γ to

$$\Gamma_x = -\bar{h}^3 \frac{\partial \bar{P}_f}{\partial \bar{x}}, \qquad \Gamma_z = -\bar{h}^3 \frac{\partial \bar{P}_f}{\partial \bar{z}}. \tag{18}$$

Additionally, the fluid supply is introduced as a source term in the center of the pad over a length of $L/40$, defined by the left-hand side of Eq. (11), while zero-pressure boundary conditions are imposed on both edges of the pad. Over the entire domain, the film height $\bar{h}$ is described by Eq. (4), coupling the deformation $\bar{w}$ from the Beam interface to the PDE interface. The translation $\bar{d}$ here is implemented through a global equation that adjusts its value until the load balance of Eq. (16) is satisfied. In this way, the PDE interface thus determines both the fluid pressure $\bar{P}_f$ and the mathematically defined pad translation $\bar{d}$.

With the translation $\bar{d}$ defined, the Beam interface remains only concerned with the pad deflections. For this purpose, the line is modeled as a floating beam element around the origin, where it is assumed that the bearing pad is kept in a horizontal position and prevented from translating in the horizontal direction by the bearing support. Instead of fixed boundary conditions, the Beam interface therefore restrains the pad to the origin with three global integral constraints defined as

$$\int_{\bar{x}=-\frac{1}{2}}^{\bar{x}=\frac{1}{2}} \bar{u} \, d\bar{x} = 0, \tag{19}$$

$$\int_{\bar{x}=-\frac{1}{2}}^{\bar{x}=\frac{1}{2}} \bar{w} \, d\bar{x} = 0, \tag{20}$$

$$\int_{\bar{x}=-\frac{1}{2}}^{\bar{x}=\frac{1}{2}} \theta_p \, d\bar{x} = 0, \tag{21}$$

where $\bar{u} = u/L$ is the deformation component in the x-direction. For the pad's deflection, the Euler–Bernoulli equation is used, which COMSOL defines by default for a limited beam width as

$$\frac{\partial^2}{\partial x^2}\left(E I_{zz} \frac{\partial^2 w}{\partial x^2}\right) = P_z, \tag{22}$$

with I_{zz} being the beam's second moment of inertia and P_z the applied pressure. With the Young's modulus fixed at 1, the input of I_{zz} is defined as $1/(12\Pi_2)$, such that the Beam interface reproduces the non-dimensional, infinitely wide formulation of Eq. (13). The cross-sectional area is additionally set to 1e6 to put the strain along the pad effectively to zero, as no effects are expected in this direction with the normal loads. By defining the cross-section manually with the I_{zz} and cross-sectional area, the thickness of the pad does not need to be specified, while it is still indirectly included in the parameter group Π_2. The loads on the pad are further applied normal to its surface based on the local pad angle θ_p. For the fluid film pressure, this requires an Edge Load with a force per unit length $\boldsymbol{F}'_{\text{edge}}$ defined as

$$F'_{\text{edge},x} = -\bar{P}_f \sin(\theta_p), \qquad F'_{\text{edge},y} = \bar{P}_f \cos(\theta_p), \tag{23}$$

which couples the fluid film pressure $\bar{P}_f$ from the PDE interface to the Beam interface. For the discrete forces of the support, the nominal force distribution $\bar{F}'_{i,n}$ is first determined at $\Pi_2 = 10^{-2}$. For this, the nominal pressure envelope $\bar{P}_{r,n}$ from Eq. (6) is applied to the underside of the pad, while the pad is fixed in the points that were defined in the geometry. The reaction forces required to maintain these positions are subsequently used as the nominal load distribution $\bar{F}'_{i,n}$, which have a negative value as they point downwards. After scaling these forces to satisfy Eq. (16), the loads $\bar{F}'_i$ are applied as point loads $\boldsymbol{F}_{\text{point}}$ by

$$F_{\text{point},x} = -\bar{F}'_i \sin(\theta_{p,i}), \qquad F_{\text{point},y} = \bar{F}'_i \cos(\theta_{p,i}). \tag{24}$$

To correctly model the non-linear deflection of the pad on larger curvatures, geometric nonlinearity is additionally activated in the study settings. With this setup, the model follows a verified approach for large beam deformations [33] and a standard Reynolds implementation as verified in earlier work [27].

To solve the presented model and to obtain convergence for varying parameter values, the numerical procedure is divided in five steps. In the first step, an initial film pressure is determined for a straight pad at the nominal film height, by setting $\bar{d} = 1$ and deactivating the loads on the pad. With this initial solution, the film pressure and support loads are activated in the second step, together with the global equation to adjust the translation $\bar{d}$. A default compliance of $\Pi_2 = 10^{-2}$ is used here to limit the magnitude of the deformations. In the third step, the deflections $\bar{w}$ are activated in the film height (Eq. (4)), which completes the system of equations. From here, the relative compliance Π_2 can be increased in steps to its desired value in step four, followed by stepwise increasing the surface curvature in step five. In all these presented steps, the physics interfaces are simultaneously solved as a Fully Coupled system by the direct MUMPS solver until a relative tolerance of 0.001 is reached.

3. Results

With the presented model, two types of analyses have been performed. The first type considers the adaptation of the pad on a flat surface for increasing compliance values Π_2. In essence, this analysis shows how the compliant, initially flat pad forms a recess in response to the discrete forces of the support, which have been correspondingly distributed and sized. Additionally, this analysis is used to show that the adaptation improves with pad compliance, which is used to establish initial design boundaries for the input parameters. The second type of analysis then evaluates the behavior and performance of the pad on increasingly curved surfaces. Here, the results from the analysis on a flat surface are used as a starting point for the simulations. Both analyses are presented in this section, together with a parametric study of the input parameters.

3.1. Adaptation on flat surface

The analysis on a flat surface is divided in two parts. First, a general example is given to illustrate the working principle. The next paragraph then shows how this result can be generalized for different input parameters and how the number of forces N_x influences this generalized result.

For the general example, a specific set of parameters is used as shown in Table 1. A mechanical land width of $\alpha_m = 1/3$ is chosen here to represent the most efficient film profile that generates the highest load capacity with the least amount of power.[1] The value of Π_1 is further based on a nominal film height of 100 μm for a bearing with a length of 100 mm, while 50 discrete forces are used for N_x to start with a finely distributed mechanical load. With these parameters, the steady state behavior of the flexible pad is simulated for increasing compliance values Π_2, as shown in Fig. 6. In this figure, the deformation is plotted in (a), next to the film pressure and nominal load profile of the discrete forces (b) and the resultant load on the pad (c). Figures (a) and (b) are animated in the digital version of this work.

Based on the figure, several effects can be seen. A relatively stiff pad (i.e. $\Pi_2 = 10^{-2}$) deforms minimally, resulting in a parallel film with a triangular pressure profile that creates a three-point type of load on the pad. At an increasing compliance, this load causes the pad to bend down at the sides, which leads to a decreasing film thickness and a change in the film pressure. At some point, this causes the resulting load to switch to a five-point type of load as seen at $\Pi_2 = 10^0$. Further increasing the compliance, this resulting load can create both a recess in the center and a parallel film towards the edges of the pad (e.g. $\Pi_2 = 10^1$). From here, the film pressure approaches the applied load profile more closely, while a smaller resulting load is needed to induce the required deformation as shown in Fig. 6(c) for $\Pi_2 = 10^3$. Eventually, the profiles of the film pressure and the applied load become so close that the bending moment in the pad oscillates around zero. Combined with a high compliance, this alternating moment initiates wavy deformations in the pad between the applied loads, which is already seen at $\Pi_2 = 10^3$ and increases with compliance.

Table 1
Parameters for the pad adaptation on a flat surface in Fig. 6.

Parameter	Description	Value
α_m	Mechanical land width	1/3
β	Pressure ratio	0.5
Π_1	Relative nominal film thickness	0.001
Π_3	Active load-ratio	1
N_x	Number of discrete forces	50

Two metrics to characterize this behavior, which are further used in this study to measure the operating performance, are the minimal film height $\bar{h}_{min}$ and the effective land width α_f. Based on the deformation, the changes in minimal film height are shown in the top right of Fig. 6(a). The initial bend in the pad causes a dip in the minimal film height before it approaches the nominal value $\bar{h}_{min} = 1$. This value is expected once the bearing is adapted, as the supply parameters are based on the assumption that the film obtains the nominal pressure profile. At larger compliancies though, $\bar{h}_{min}$ drops again, which indicates the onset of the oscillations in the deformation. Yet to measure if the pad converged to the imposed mechanical land width (α_m), an additional metric is required. In deformable bearings, however, the land width is difficult to define because the film profile is curved [27] rather than sharply shaped as in Fig. 2(a). The effective land width is therefore used [27], which indirectly measures the land width as the distance over which the film pressure drops from 95% to 5% of the recess pressure. Based on this definition and the pressure distributions in Fig. 6(b), the land width develops as shown in the top right of this same figure.

3.2. Parameter study on flat surface

The results from the previous section can be generalized for a range of combinations of the input parameters by several master curves. For the parameters α_m, β, Π_1 and Π_3 this is shown in Fig. 7, where the development of the land width and minimum film height are respectively presented in sub-figures (a) and (b). Here, a fixed number of discrete forces of $N_x = 50$ is used. To obtain these master curves, the effects of Π_1 and Π_3 are combined with Π_2 into a single scaling parameter on the x-axis, which follows from the overview in Fig. 5. On a flat surface, there is no input from the surface shape $\bar{z}_t$. This means that only the deformation affects the film profile, where Π_2 linearly scales the deformation $\bar{w}$ while Π_1 inversely scales the influence of this deformation on the film height $\bar{h}$. Hence, equal ratios of Π_2/Π_1 give the same result. Load-ratio Π_3, however, influences the results in two ways. Firstly, it determines the magnitude of the pressure envelopes and the difference between them, as both loads in Eqs. (15) and (16) scale linearly with Π_3. Similar to Π_2, this influences the deformation $\bar{w}$ in Eq. (13). So, for an equal product of $\Pi_2 \cdot \Pi_3$, the deformation $\bar{w}$ and its influence on the film height $\bar{h}$ should stay the same. Secondly, the load Π_3 also influences the average fly height $\bar{d}$ of the pad, which in turn affects the impact of the deformations on the film profile $\bar{h}$ in a similar way as the nominal film thickness Π_1. To correct for this effect, the group $\Pi_2\Pi_3/\Pi_1$ is divided by the theoretically expected film thickness due to any deviations from $\Pi_3 = 1$. This results in the second term in the x-axes, of which the derivation is further given in Appendix A. The combined parameter group on the x-axis is referred to as the "generalized compliance", which physically represents the deformation of the pad under the active load F' relative to the film thickness.

[1] Similar to the optimum in a circular hydrostatic bearing [1], this optimum is found in 2D by multiplying the supply pressure (Eq. (7)) with the nominal flow (right hand side of Eq. (9)) to get the power for the nominal load. Differentiating this power to α_m and equating to zero gives a minimum power at $\alpha_m = 1/3$.

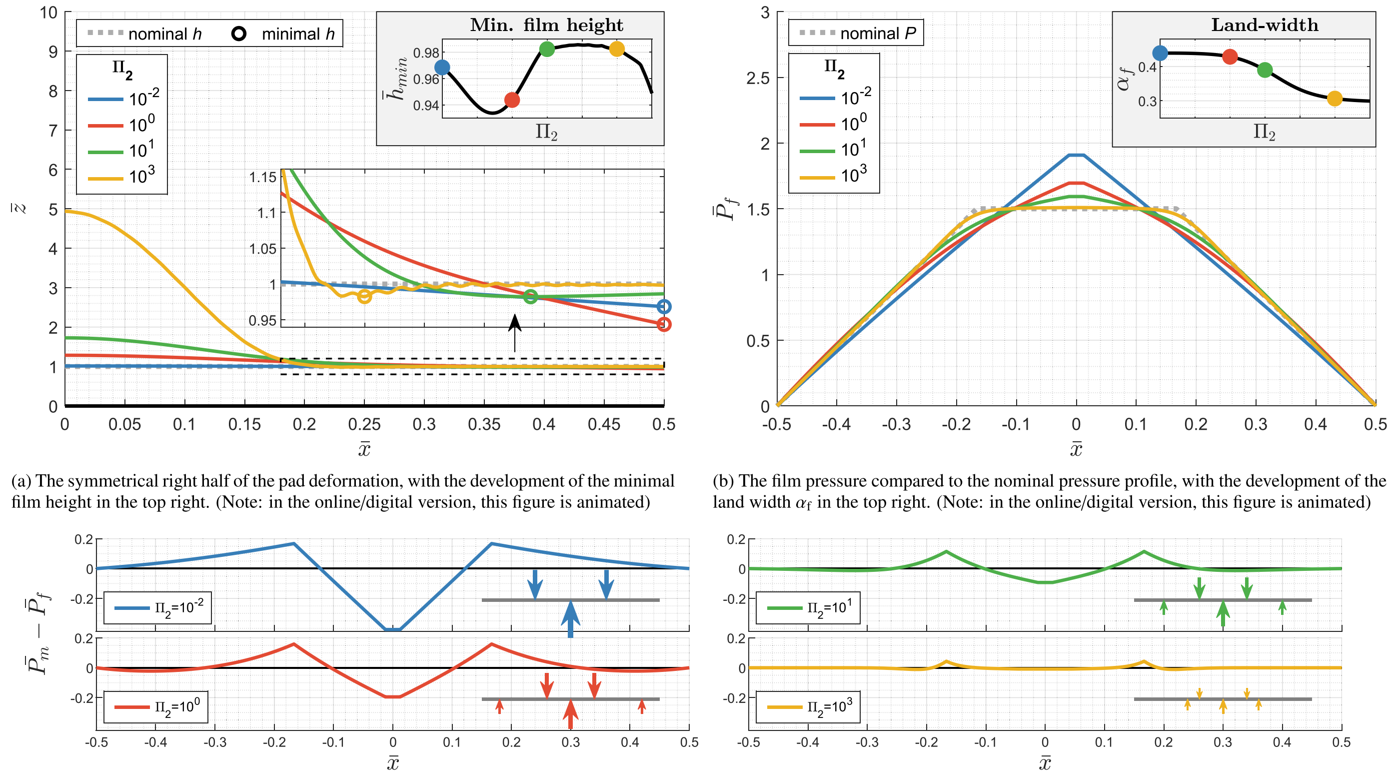

(a) The symmetrical right half of the pad deformation, with the development of the minimal film height in the top right. (Note: in the online/digital version, this figure is animated)

(b) The film pressure compared to the nominal pressure profile, with the development of the land width α_f in the top right. (Note: in the online/digital version, this figure is animated)

(c) Resulting pressure profile acting on the pad, with a schematic depiction of the load situation in the bottom right corner of each graph.

Fig. 6. Adaptation of the flexible pad on a nominally flat surface for increasing compliance values Π_2, with the input parameters as defined in Table 1.

With the generalized compliance, the results only depend on the land width and pressure ratio in Fig. 7. Next to a land width of 1/3, the adaptation of the pad is shown for a parallel film with $\alpha_m = 0.45$ and for larger recessed films with a land width of 0.25 and 0.15. Similar to the trend shown in Fig. 6(b), the pad approaches the imposed land widths in Fig. 7(a) for an increasing generalized compliance. Here, it must be noted that each line converges to a slightly lower value than α_m, as the α_f-metric by definition cuts 10% of the pressure drop to exclude any decrease in pressure in the recess or a diverging film at the outer edges of the land width [27]. With respect to the minimal film height in Fig. 6(a), however, a different behavior is seen for different land widths in Fig. 7(b). At the nominal load of $\Pi_3 = 1$, the initial dip in the minimal film height is almost absent for the parallel film with $\alpha_m = 0.45$. In this situation, the initial straight pad already has the desired shape for a parallel film at a low compliance. Hence, there is no difference between the applied load and the film pressure that bends the tips of the pad downwards at larger compliancies, giving a film thickness directly close to $\bar{h}_{min} = 1$. At land widths smaller than 1/3 though, the pad actually needs a larger generalized compliance to form a parallel film in the land width region. This is seen in the bottom graph of Fig. 7(b) by a later stabilization of the minimum film height. For loads other than $\Pi_3 = 1$, the film height changes to adjust the pressure drop over the restrictor, like in regular hydrostatic bearings. Yet it is important to note in the first graph of Fig. 7(b) that the film height of $\alpha_m = 1/3$, and thereby its film profile, stabilizes around a generalized compliance of 10^4 for each of the relative loads Π_3. This value is therefore used as a general minimum for the input parameters in later analyses. Regarding the influence of β, two observations need to be mentioned. First of all, it is seen in Fig. 7(a) that β does not influence the adaptability of the pad in terms of the land width, which mainly depends on the pad stiffness and load profiles. It does, however, influence the film thickness in the adapting phase as seen in the bottom graph of Fig. 7(b), but only to the point where the lines approach $\bar{h}_{min} = 1$. From that point, the pad behaves like a regular bearing with its target land width α_m, where the pressure ratio only influences the film stiffness.

Similar to Fig. 7, the effect of the number of support forces N_x is shown in Fig. 8. Here, two important effects can be noted by looking at the minimum film height in the upper graph of Fig. 8(b). In the adaptation phase, like in the valley of $\alpha_m = 1/3$, the lines overlap for different N_x-values. Hence, the minimum generalized compliance to approach the desired film profile is not influenced by the discretization of the support. The number of forces does however influence the generalized compliance at which the film thickness starts to drop. With fewer forces, the segment length between the forces and the load that each segment needs to carry becomes larger. As a result, the pad deforms between the discrete forces at a lower compliance, which initiates the decrease in film thickness. Once the deformations become larger, they start to influence the film pressure as well, resulting in a deviation of the effective land width as seen in Fig. 8(a). The onset of these effects can be predicted though, by correcting the load F' and length L in the generalized compliance to a load and length per unit segment. Substituting the groups from Eq. (17), it follows that $\Pi_2\Pi_3/\Pi_1$ scales with $F'L^3$. Neglecting the relative small influence of the second term in the generalized compliance, the input can thus be corrected by N_x^4, of which the result is shown in the bottom graph of Fig. 8(b). Here it is seen that the onset of the wavy deformations occurs around a corrected generalized compliance of 10^0. Hence, this value is used as a maximum for the input parameters in the last two paragraphs for the behavior on curved surfaces.

3.3. Adaptation on increasing curvatures

The performance analysis on increasing curvatures is again divided in two parts. Similar to Section 3.1, a general example is first given to illustrate the effects that play a role in this situation. Next, this result is expanded for varying parameters to analyze the overall potential performance. Following [27], a dimensionless curvature $\bar{k}$ is used here to define the unevenness of the surface relative to the bearing size, defined as $\bar{k} = L/R_t$.

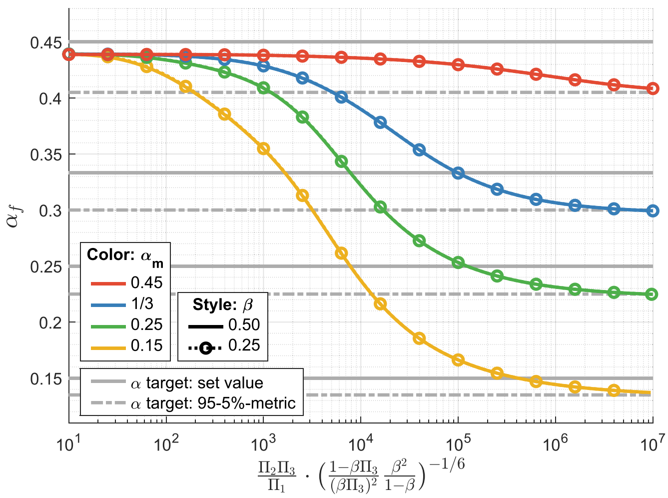

(a) Development of the effective land width α_f for an increasing generalized compliance. For each imposed land width α_m, the target value and its corresponding value under the definition of the metric for α_f (i.e. the length over which the pressure drops from 95% to 5% of the recess pressure) are plotted with the grey, horizontal target-lines.

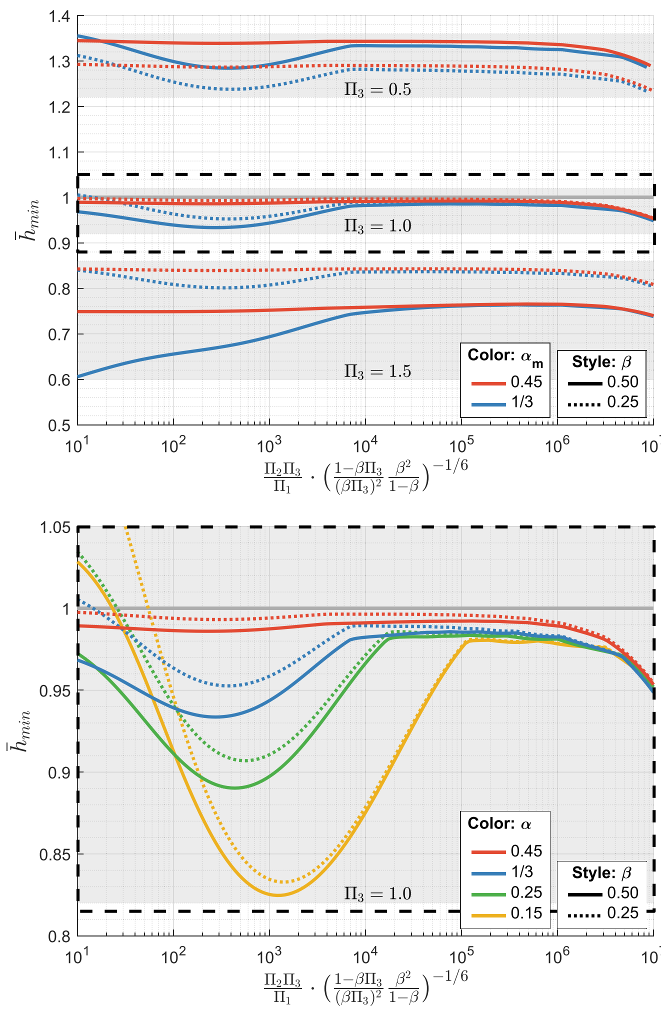

(b) Development of the minimal film height $\bar{h}_{min}$ for an increasing generalized compliance. In the top figure, h_{min} is shown for three specific loads of Π_3, as the film height strongly depends on the load on the pad. For $\Pi_3 = 1$, the result is enlarged in the bottom figure, where the effects of two smaller values for the imposed land width α_m are added.

Fig. 7. Influence of the input parameters α_m, β, Π_1 and Π_3 on the adapting behavior of the flexible pad on a flat surface, using $N_x = 50$. The influence of Π_1 and Π_3 is combined here with the increasing compliance Π_2 on the x-axis.

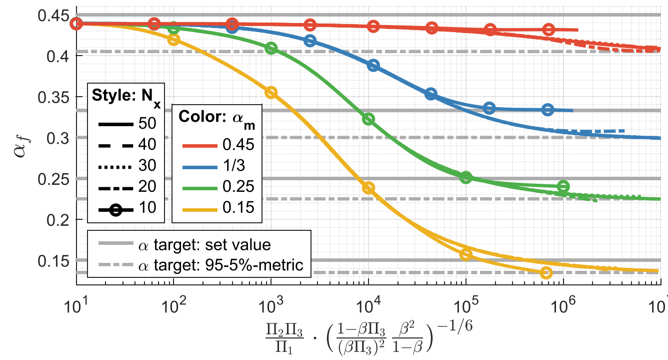

(a) Development of the effective land width α_f for an increasing generalized compliance.

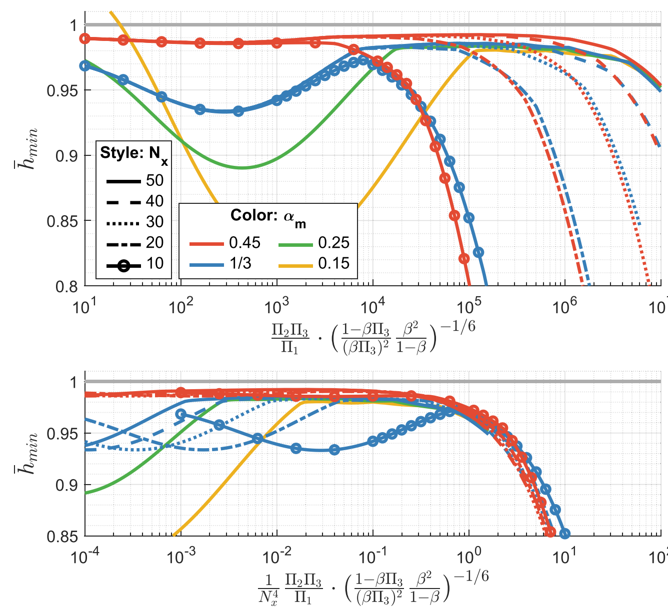

(b) Development of the minimal film height $\bar{h}_{min}$. In both figures, the result is plotted versus the generalized compliance. In the bottom figure, however, the x-axis is corrected with the number of forces N_x for an equal load en length per segment between the forces. The results of the land widths of 0.15 and 0.25 are only plotted for $N_x = 50$ for clarity in the graph, as their behavior is similar to that of the land widths 1/3 and 0.45.

Fig. 8. Influence of the number of discrete forces N_x on the adapting behavior of the flexible pad on a flat surface, using $\beta = 0.5$.

In the general example, the adaptation of a specific design is evaluated for increasing curvatures $\bar{k}$. For this, the parameters from Table 1 are used again, together with $\Pi_2 = 10^1$. This value is specifically chosen to set the generalized compliance of the example to the minimum value of 10^4, since a stiff design most clearly illustrates the limitations in adaptability. With the given parameters, the steady state behavior at different curvatures is shown in Fig. 9. Here, sub-figure (a) shows an example of the pad deformation relative to the surface and defines the meaning of the terms ‘convex’ and ‘concave’ as used throughout this study. The height and pressure profile of the film at three curvatures is subsequently presented in sub-figures (b) and (c). To illustrate the magnitude of the curvature $\bar{k}$ in these graphs, four example surface profiles are presented to scale in Fig. 10. Based on the results, a general pattern can be seen in the adaptation of the pad. Starting with the deformation in Fig. 9(a), it is observed that the tips of the pad are always straight. This is also expected as no bending moment can be present in these tips due to the absence of any boundary loads (see Eq. (14)). As a result, the pad needs to build up an internal bending moment from the tips inwards to adapt itself to the surface curvature, which is possible by a difference between the applied support load and film pressure. On convex surfaces, as seen on the left in Fig. 9(a),

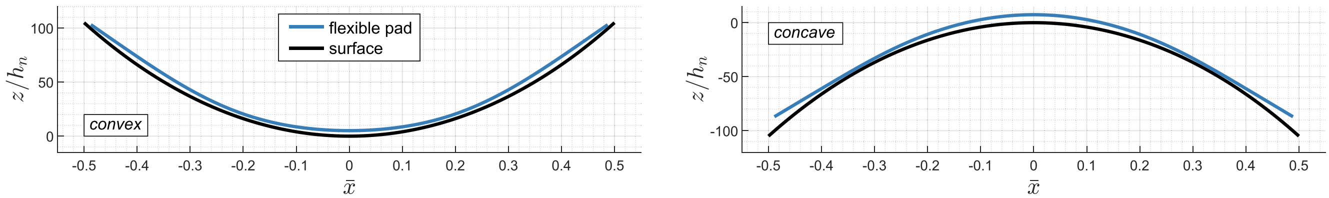

(a) Examples of the pad adaptation to a curved surface at the maximum simulated curvature of $\bar{k} = 0.8$. To visualize the relative adaptation, the film thickness is slightly exaggerated.

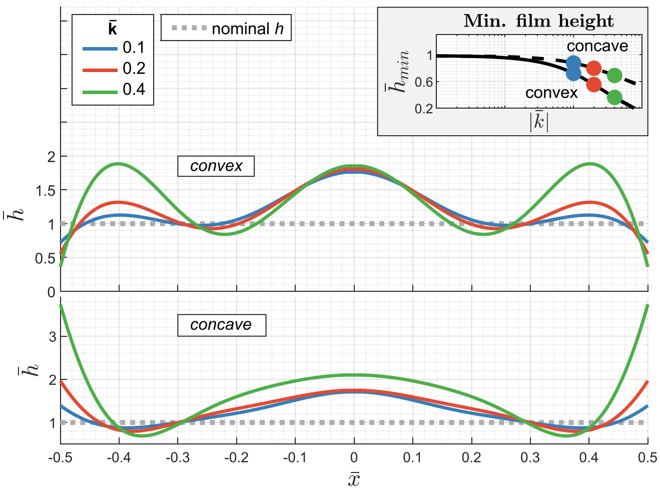

(b) The film thickness profile compared to the nominal film thickness at three specific curvatures, with the schematic development of the minimal film height in the top right.

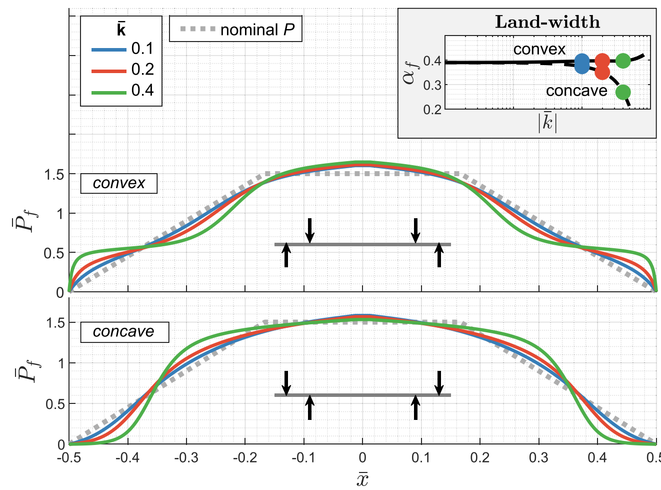

(c) The film pressure compared to the nominal pressure profile and the resulting type of load, with the schematic development of the land width α_f in the top right.

Fig. 9. Adaptation of the flexible pad on increasing convex and concave curvatures, with the input parameters as defined in Table 1 and a compliance of $\Pi_2 = 10^1$.

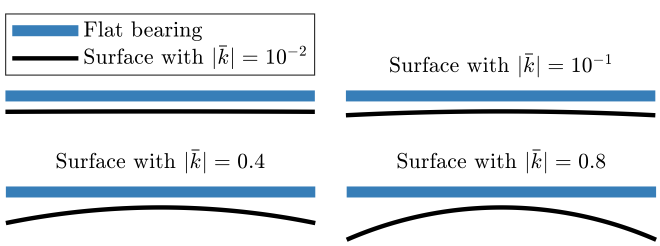

Fig. 10. Examples of the surface curvature on scale for different magnitudes of $\bar{k}$.
Source: Reproduced with permission from Sonneveld and Ostayen [27].

Table 2
Overview of the parameter combinations plotted in Figs. 11(c) and 11(d).

Π_2	Π_1: 10^{-4}	10^{-3}	10^{-2}
10^0	Blue ▽		
10^1		Blue (default)	
10^2	Green ▽	Orange (default)	Blue ⊿
10^3		Green (default)	Orange ⊿

this results in a stronger curvature around $\bar{x} = 0.2$, after which a straighter section of the pad creates a slightly thicker film before the tip approaches the surface again. Based on this film profile, also shown in Fig. 9(b), the film pressure becomes successively larger and smaller from the tips inwards, as seen in Fig. 9(c). Effectively, this creates two opposite resultant pressure areas that induce a bending moment in the rest of the pad. On concave surfaces, a similar effect can be seen in the right of Fig. 9(a), although the tips now diverge from the surface. In this way, the film pressure decreases near the tips and increases shortly after, creating an opposite bending moment that adapts the pad to a concave shape. In both cases, the presented effects increase in magnitude at larger curvatures to generate a larger bending moment for the pad.

The changes in the film profiles and pressures also influence the performance in terms of the minimum film height and land width. The minimum film thickness decreases on both convex and concave surfaces, although for different reasons. On convex surfaces, the straight tips point towards the surface, while on concave surfaces the overall fly height decreases as the load is effectively carried by a smaller pad segment. Based on these changes in the pressure profiles, the land width respectively increases and decreases on convex and concave surfaces. These behaviors are schematically shown in the top right of Figs. 9(b) and 9(c), and further expanded in the following section.

3.4. Parameter study on varying curvatures

This section extends the results from the previous example to a wider range of parameter combinations to finally analyze the potential performance of the flexible pad. First, it must be noted however that a generalization of the results, as shown with the generalized compliance on a flat surface, is no longer possible. The main reason for this is the presence of the imperfections in the film profile on larger curvatures. For example, the straight tips of the pad will always converge towards the surface on a convex profile, as no bending moment is available to curve them along the surface. Yet at different nominal film heights Π_1, this will have a different influence on the decrease in dimensionless film thickness. On a flat surface, this was not a problem as the tips always extended parallel along the surface once the pad is fully adapted. Hence, Figs. 11(a) and 11(b) first show the results for the effective land width and minimum film thickness for different compliancies Π_2 at a nominal film height of $\Pi_1 = 10^{-3}$. Selective variations of the parameters Π_1 and Π_2 are subsequently presented in Figs. 11(c) and 11(d), with an overview of the combinations that are plotted given in Table 2.

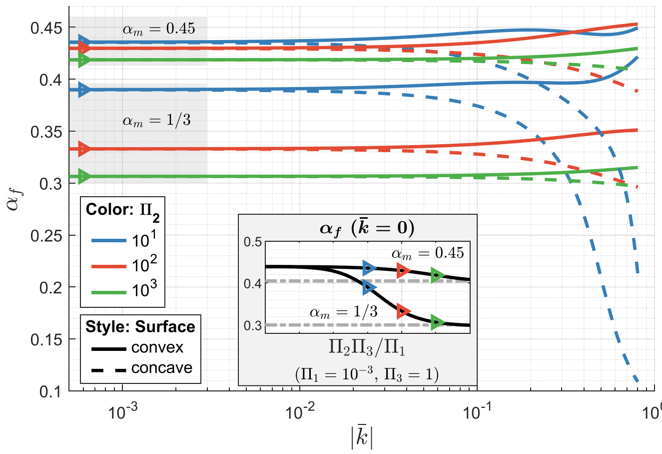

(a) Development of the effective land width α_f for $\Pi_1 = 10^{-3}$. The inserted figure in the bottom shows the land width as a function of the generalized compliance on a flat surface, indicating the parameters and starting points used here for the analysis on curvatures.

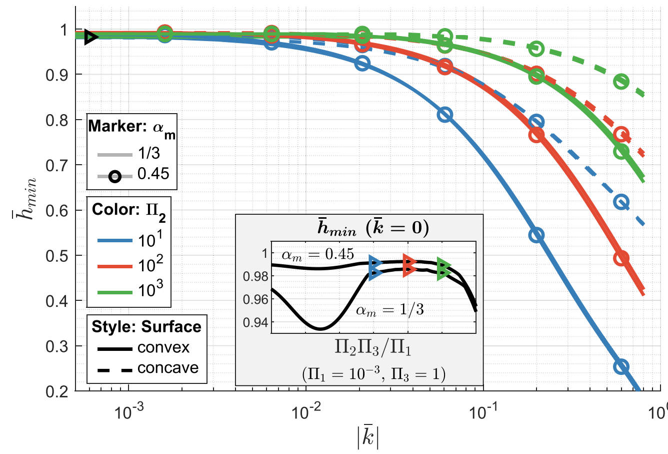

(b) Development of the minimum film height $\bar{h}_{\min}$ for $\Pi_1 = 10^{-3}$. The inserted figure in the bottom shows the minimum film height as a function of the generalized compliance on a flat surface, indicating the parameters used here for the analysis on curvatures.

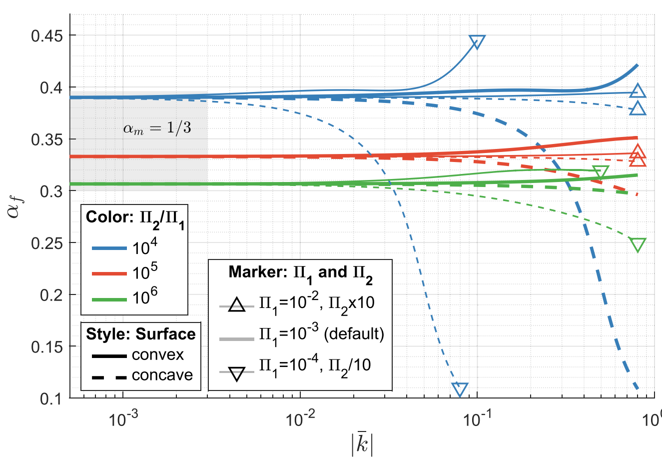

(c) Development of the effective land width α_f for varying combinations of Π_1 and Π_2. An overview of the parameter combinations that are plotted is given in Table 2.

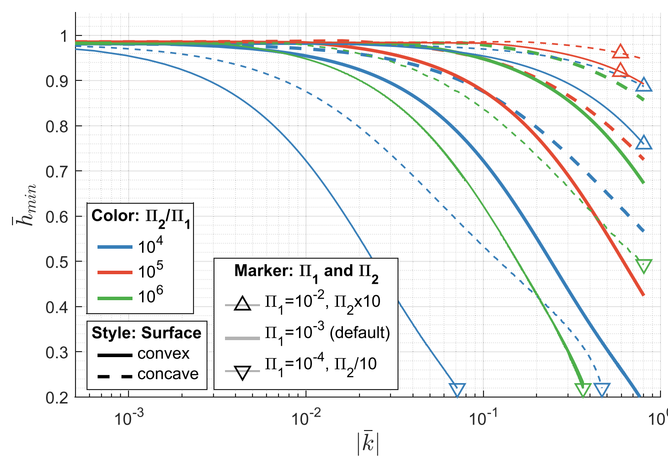

(d) Development of the minimum film height $\bar{h}_{\min}$ for varying combinations of Π_1 and Π_2. An overview of the parameter combinations that are plotted is given in Table 2.

Fig. 11. Adaptation of the flexible pad on increasing convex and concave surfaces, using $\beta = 0.5$, $\Pi_3 = 1$ and $N_x = 50$.

Starting at Figs. 11(a) and 11(b), the development of the effective land width and minimum film thickness is shown for increasing curvatures on both a convex and concave surface. Here, the inset figures provide a recap of the metrics on a flat surface, to clarify the different starting points of each line. Accordingly, the values of Π_2 are chosen within the limits of the generalized compliance that were set in Section 3.2. Based on both graphs, it is seen that performance improves with increasing compliance. In Fig. 11(a), this is seen by smaller deviations of the land widths compared to their initial values at $\bar{k} = 10^{-3}$, while in Fig. 11(b) it is seen by a smaller decrease in the minimum film thickness. This behavior is also expected as more compliant pads require less pressure to be deformed, which means that a smaller deviation from the intended film profile suffices to generate the necessary resulting pressure on the pad. For both the parallel film and recessed film with $\alpha_m = 1/3$, the effective land width changes maximally 4% up to a curvature of $\bar{k} = 0.8$ for a compliance of $\Pi_2 = 10^3$. Additionally, the minimum film thickness drops at most to $\bar{h}_{\min} = 0.66$ with these parameters on the convex surface, which always suffers the largest drop due to the straight tips as shown in Fig. 11(b).

Taking the results of $\alpha_m = 1/3$ in Figs. 11(a) and 11(b) as a baseline, several parameter variations of Π_1 and Π_2 are shown in Figs. 11(c) and 11(d). To analyze the influence of Π_1 from these figures, it is important to note that the equally colored lines with the same generalized compliance differ in both Π_1 and Π_2, as shown in Table 2. Hence, the three line styles for $\Pi_2 = 10^2$, indicated in the third row of Table 2, are considered first. Based on Fig. 11(c), the influence of Π_1 seems limited, with only a slight difference in the curvature at which the land widths start to deviate from their initial value. Yet in Fig. 11(d), a significant improvement in performance is seen between the three lines, indicating that a larger nominal film thickness reduces the decline in film height at stronger curvatures. As mentioned in the introduction of this section, this can be explained by the fact that the imperfections in the pad adaptation have less influence at a larger film thickness. Considering the results for a constant generalized compliance, for example that of $\Pi_2/\Pi_1 = 10^4$, it can also be seen that the effects of Π_1 and Π_2 are cumulative. At the smaller film thickness of $\Pi_1 = 10^{-4}$ and a compliance of $\Pi_2 = 10^0$ (blue ∇), the performance starts to decline already at curvatures between 10^{-3} and 10^{-2}. Yet for $\Pi_1 = 10^{-2}$ and $\Pi_2 = 10^2$ (blue Δ), the performance in terms of the decline in minimum film thickness is even slightly better than that of the default green line, which uses a ten times larger compliance in combination with a ten times smaller nominal film thickness. Based on these observations that larger values of Π_1 and Π_2 improve the adaptation of the pad, a set of general design rules for Π_1 and Π_2 will be presented in the discussion.

Apart from Π_1 and Π_2, the input parameters further consist of the pressure ratio β, the number of forces N_x and the active load-ratio Π_3. These parameters, however, showed no influence (β, N_x) or only a minimal influence (Π_3) on the performance of the pad on curved surfaces, as presented in this section. Hence, the results for variations in these parameters are provided in the supplementary material with this publication.

4. Discussion

This work extends the application of the load-based approach for pressure profile matching to the development of deformable fluid film bearings that can operate on larger surface curvatures. To do so, it focuses on the feasibility of the approach with respect to two practical limitations: the discretization of the support load and the influence of the pad compliance. In this section, the concept and approach are discussed, followed by the results, design rules and generalization of the study.

4.1. Concept and model approach

The presented concept to apply the desired pressure profile with a load-distributing support differs from previous pressure-profile-matching approaches in two important ways. With such a load-distributing support, the pressure profile is no longer based on a pre-compression of elastic elements, like the rubber support from Fig. 2(b) in [14] or the array of compression springs used in [28]. As a result, the load distribution on the pad and the overall compression of the support become independent of the load on the bearing itself. This allows the bearing load to vary in applications such as cam-follower systems without changing the prescribed support load distribution. Eventually, this can also improve the adaptability and the tracking performance of the bearing under varying conditions. The second unique property of the load-distributing support is the potential to apply the load closer to the normal direction of the pad's surface. In a rubber support like Fig. 2(b), for example, there is a strong coupling between the deformations in the x and z direction that influence the resulting pressure profile [14]. Similarly does the use of vertical springs in [28] only control the load profile on a horizontal plane. With a differential mechanism as introduced in Fig. 2(c), it might be possible to act more perpendicular on the pad, independent of its shape. To identify the potential of this approach, the study focused on the pad's reaction to such an idealized load distribution.

With respect to the model for this pad behavior, two choices are discussed. The first choice relates to the distribution of the forces, which are placed in the center of N_x equally spaced pad segments as shown in Fig. 4(c). For different load profiles and on different surface shapes, a more optimal distribution might exist that uses different segment lengths and varying locations of the forces within these segments. Yet with varying curvatures, this optimal distribution is expected to change constantly. For this reason, the equidistant distribution of the forces is used as an average solution. The second model choice relates to the tangential strain in the pad, which is assumed to be equal to zero in the analyses by using a large cross sectional area in the COMSOL model. Under the assumption that the discrete support forces always act perpendicular to the surface, this assumption of zero tangential strain is acceptable. In this case, both the fluid film pressure and the distributed support load rotate with the deformations of the pad, which prevents the buildup of tangential stresses and the associated strains. However, if the load-distributing support is not able to apply the load perfectly normal to the pad, compressive or tensile loads could arise in the pad. In this situation, tensile loads are desired over compressive loads to prevent the pad from folding inwards and to keep its surface stretched. Still, this tensile load will pull the subsequent points on the pad away from each other, creating a geometric stiffening effect that makes it harder for the pad segments between them to bend. Hence, the results in this work represent the theoretical optimum of the achievable adaptability of the pad. In practical implementations with non-perpendicular load profiles, larger deviations in the film and pressure profile will be required to adapt to similar curvatures, which increases with the tensile stress in the pad. To model this effect, Eq. (13) could be extended in future work with a tensile force component as in the Föppl-von Kármán equations, which describe the large deflections of thin plates in tension [34,35].

4.2. Results

With the model, the performance of the flexible pad has been analyzed in Section 3, the results of which are further discussed here. Starting with the analyses on a flat surface, it is noted that the performance is defined by how well the pad adapts to the intended pressure profile and corresponding film height distribution. As the minimum film height approaches the nominal value of $\bar{h}_{\min} = 1$ in Fig. 7(b), it becomes clear that defining the supply parameters based on the nominal operating condition is effective. The film height, however, does not exactly reach $\bar{h}_{\min} = 1$ as a slight deviation in the film and pressure profile is required to initiate the pad deformation. Once wavy deformations start to occur in the pad, as indicated by the decline in the minimum film thickness, these changes are not directly visible in the film pressure. At larger compliancies though, the deformations between the discrete force locations keep increasing, which could eventually disturb the laminar flow and influence the bearing performance. Hence, the decline in minimum film thickness is taken into account for the design rules in Section 4.3.

Additionally, it was noted that the pressure ratio β in Fig. 7(b) only influences the adaptation of the pad to the point where the minimum film thickness approaches $\bar{h}_{\min} = 1$. Up to this point, the pad has not sufficiently adapted to form the nominal film profile. In response, the pad requires a different film height than $\bar{h}_{\min} = 1$ to generate the required load capacity. Because the pressure ratio β determines the film stiffness, the required change in film thickness depends on the value of β up to this point. Once the pad has adapted, however, the pressure ratio only defines the film stiffness as in regular bearings. For this reason, no variations in the pressure ratio have been considered in further analyses.

Subsequently, the performance has been analyzed on curved surfaces. In contrast to the flat-surface case, performance is defined here by how well the pad is able to maintain its initial adaptation on larger curvatures. For this, it should first be noted that the metrics are not perfect. A decrease in the minimum film thickness, for example, could just be the tip of the pad that approaches the surface instead of the entire bearing, as seen for $\bar{k} = 0.1$ on a convex surface in Fig. 9(b). Conversely, the land width does not seem to change significantly on a convex surface for $\bar{k} = 0.4$ in Fig. 9(c), while a second recess has formed towards the edge of the bearing in Fig. 9(b). In both cases, however, the bearing is expected to remain operational due to the presence of a continuous thin film without excessively large pockets or constrictions. An initial deviation from the nominal performance thus mainly indicates the onset of a different type of behavior, rather than a direct and significant loss of performance.

With this interpretation of the performance metrics in mind, the results can be compared to previous studies. The load-based approach for pressure profile matching was previously introduced in [28] with only a vertically oriented load distribution, where the adaptation was analyzed up to a maximum curvature of $\bar{k} = 0.02$.[2] The present work has extended this concept to larger curvature deformations, which shows that adaptations can be achieved up to $\bar{k} = 0.8$ by applying the load normal to the pad surface. Compared to alternative deformable bearing concepts, the improvement is similarly significant. The stiffness-based approach shown in the left of Fig. 3 was analyzed up to a curvature of $\bar{k} = 0.0032$, at which the minimum film thickness had already decreased to roughly 20% of its nominal value [14]. The closed-cell bearing concept from [27] was shown to operate up to a significantly larger curvature of $\bar{k} = 0.4$, but with a land width of approximately $\alpha_m = 0.05$, resulting in a substantially higher flow rate and power consumption. In contrast, the present simulations show that a land width of approximately $\alpha_m = 1/3$ can be maintained up to $\bar{k} = 0.8$,

[2] This curvature is based on the parameters in [28]: a pad length of 50 mm and a sinusoid with a wavelength of 250 mm and an amplitude of 750 μm.

while the minimum film thickness remains above $\bar{h}_{\min} = 0.66$. These results indicate that the load-based approach can achieve both a larger curvature adaptation range and a more favorable film geometry than previously reported deformable bearing concepts.

Nevertheless, it should be noted that the performance still depends on the ratio between the stiffness of the pad and the bearing load in Π_2. In Fig. 11(a) though, it can be seen that an operable performance at the larger curvatures can be achieved for both a compliance of $\Pi_2 = 10^2$ and 10^3. Given a fixed set of parameters that define the stiffness of the pad, this means that a load range of a factor 10 could be accommodated while maintaining a comparable land width. Yet to achieve this in a practical bearing setup, the supply will need to actively adapt and the parameters of the pad will need to be chosen carefully with respect to the expected bearing loads.

4.3. Design rules

Based on the non-dimensional formulation of the model and the presented results, a set of design rules can be derived for the input parameters. Starting with a flat surface, it was shown that a stable region exists in the generalized compliance where the minimum film thickness approaches its nominal value. For a land width of $\alpha_m = 1/3$ and 0.45, this region is defined by

$$\frac{\Pi_2 \Pi_3}{\Pi_1} \cdot \left(\frac{1 - \beta \Pi_3}{(\beta \Pi_3)^2} \frac{\beta^2}{1 - \beta} \right)^{-1/6} > 10^4, \tag{25}$$

$$\frac{\Pi_2 \Pi_3}{\Pi_1} \cdot \left(\frac{1 - \beta \Pi_3}{(\beta \Pi_3)^2} \frac{\beta^2}{1 - \beta} \right)^{-1/6} < N_x^4. \tag{26}$$

Here, Eq. (25) defines the minimum generalized compliance that is required for the nominal film thickness to stabilize, whereas Eq. (26) defines the maximum corrected generalized compliance before wavy deformations arise. These boundary relations also imply that the number of support points, and thus pad segments, should at least be equal to 10. For smaller values of the land width, it is noted that a higher generalized compliance is needed in Eq. (25) to approach the nominal film height, as seen in Fig. 7(b). This effect is explained by the necessity for a sharper bend in the pad closer to its edge, to keep the tip of the pad horizontal while the recess starts close by. To use the given ranges in the design process, the minimum expected value of the load ratio Π_3 should be used in Eq. (25) and its maximum expected value in Eq. (26). Within the parameter range itself, a higher generalized compliance is desired to approach the intended land width and the corresponding flow conditions, as seen in Fig. 7(a). For this, a higher compliance Π_2 and a smaller nominal film thickness Π_1 are thus beneficial. With respect to Π_1, a smaller value performs better on flat surfaces because smaller pad deformations are required to produce the desired changes in the film pressure. For increasing curvatures, however, this desired optimization direction of Π_1 needs to be reconsidered.

With the parameter study in Section 3.4, it was observed that both a larger compliance Π_2 and a larger film thickness Π_1 improve the performance on curved surfaces. Here, the larger film thickness is beneficial as it reduces the impact of the pad's imperfect adaptation. Based on the surface curvatures of the application and the desired operating conditions, the film thickness can thus be optimized. Other considerations for this include the increase in flow and power associated with a larger film thickness, while a larger Π_1 also allows a larger drop in the dimensionless film height $\bar{h}$ before an absolute minimum film thickness is reached. Hence, a viable strategy would be to start with a medium film thickness and compliance that are on the boundary of Eq. (26). From there, both values can be increased simultaneously until the desired performance at the maximum curvatures is obtained with the smallest film thickness possible. A larger number of discrete forces N_x can help here to allow for larger compliancies.

4.4. Generalization

The dimensionless formulation of the model already generalizes the results of this study for hydrostatic bearing implementations and circular curvatures. The results and the presented principle, however, are expected to extend to other implementations as well. With respect to the surface shape, the largest deviation from the nominal pressure profile is required to adapt the pad to the overall curvature of the surface. Any local changes in curvature beneath the bearing, as seen in sinusoidal shapes, will thus only require a smaller pressure deviation of the film to modify the curvature of the pad over its length. Important to note though, is that the flexible pad is assumed to cover only a segment of the sinusoidal surface in this case, with the goal to track its oscillations over distance. The fundamental working principle of the load-distributing support is also expected to extend to other pressure profiles. On a smaller scale, this was already shown for hydrodynamic profiles [28]. Deviations from the intended load profile are likewise expected to be permissible, provided that the resulting load profile remains physically realizable by the fluid film pressure. For hydrostatic bearings, for example, this implies that the pressure profile should always be monotonically decreasing from the supply outwards. Depending on the relative compliance, however, this will of course affect the bearing performance. Additionally, if the load-distributing support does not apply its load normal to the surface, a tensile load may occur in the pad. If sufficiently large, this load could induce a geometric stiffening effect that reduces the flexibility of the pad, as discussed before. Investigating this effect and experimentally validating the presented concept are therefore important directions for future work.

5. Conclusion

In this work, the load-based approach for pressure-profile matching in deformable fluid film bearings is extended to hydrostatic bearings and surfaces with a significant and functional curvature. The approach assumes a discretized load-distributing support that applies the bearing load at discrete locations on a flexible pad. The local reaction forces are prescribed to match the desired film-pressure profile and act normal to the pad surface. Accordingly, the pad will try to match the film pressure to the imposed load by adapting its shape relative to the surface, which makes the bearing adaptable to varying surface curvatures. A dimensionless design model is presented for a hydrostatic implementation, which determines the steady state behavior on these curvatures for a minimum set of parameter groups. With this model, it is shown that parallel and varying recessed film profiles can be achieved with the flexible pad, for which the degree of adaptation mainly depends on the nominal film thickness and bearing load relative to the length and stiffness of the pad. Adaptation is achieved through a small deviation from the nominal film profile, which creates a difference between the applied load distribution and the film pressure. The resulting load imbalance deforms the pad until a new equilibrium is reached. At larger curvatures, this required offset and thereby the decline in performance increase, although a maximum deviation of 4% from the intended land width and a maximum drop to 66% of the intended film thickness were obtained up to curvatures of $\bar{k} = 0.8$ for the reference parameter set considered in this study. Hence, the load-based approach enables the development of deformable fluid bearings that can maintain an efficient film profile on varying curvatures, extending the demonstrated operating range of previous deformable bearing concepts. Based on the results, three design rules have been derived that can be used as a starting point for the design parameters of the pad.

CRediT authorship contribution statement

Dave D. Sonneveld: Writing – original draft, Visualization, Software, Methodology, Investigation, Formal analysis, Conceptualization. **Ron A.J. van Ostayen:** Writing – review & editing, Supervision, Methodology, Conceptualization.

Funding sources

This research did not receive any specific grant from funding agencies in the public, commercial, or not-for-profit sectors.

Declaration of competing interest

The authors declare that they have no known competing financial interests or personal relationships that could have appeared to influence the work reported in this paper.

Appendix A. Master curves: film thickness correction

The generalization of the parameter study on a flat surface in Section 3.2 is based on the influence of the deformations $\bar{w}$ on the film profile $\bar{h}$. The interaction between these parameters is also schematically shown in Fig. 5. One step of the generalization is to predict the film thickness under different load ratios of $\Pi_3 = F'/F'_n$. In the handbook of Rowe [1], a general equation is presented for this in Table 7.1 and Fig. 7.4, although with a different definition of the parameters, by

$$\bar{X}^6 = \frac{1-\bar{P}_r}{\bar{P}_r^{\,2}}\frac{\beta^2}{1-\beta}, \tag{A.1}$$

where $\bar{X}$ represents the film thickness relative to the nominal film height, similar to this study. The load and recess pressure $\bar{P}_r$, however, are defined here as a number between 0 and 1 to represent the entire load range. At the nominal condition $\bar{X} = 1$, the recess pressure $\bar{P}_r$ is equal to β. Relative to this starting point of $\bar{P}_r = \beta$, the loads can be increased or decreased, which is defined in this model by the active load ratio Π_3. Hence, $\bar{P}_r$ in Eq. (A.1) can be replaced by $\beta \cdot \Pi_3$. Taking the sixth root of this equation then gives the prediction of the film height at different values of the load ratio Π_3.

Appendix B. Supplementary data

Supplementary material related to this article can be found online at https://doi.org/10.1016/j.triboint.2026.112530.

Data availability

The models and code related to this publication are available in the 4TU.ResearchData respository, DOI: 10.4121/3fb28ed6-f59e-4163-beaa-9960968f0a6c.

References

[1] Rowe WB. Hydrostatic, aerostatic and hybrid bearing design. first ed.. Elsevier; 2012.
[2] Colechin M, Stone C, Leonard H. Analysis of roller-follower valve gear. In: SAE technical paper 930692. 1993, p. 75–84. http://dx.doi.org/10.4271/930692.
[3] Lee J, Patterson D. Analysis of cam/roller follower friction and slippage in valve train systems. In: SAE technical paper 951039. 1995, p. 65–72. http://dx.doi.org/10.4271/951039.
[4] Ji F, Taylor CM. A tribological study of roller follower valve trains. part 1: A theoretical study with a numerical lubrication model considering possible sliding. In: Tribology series. vol. 34, Elsevier; 1998, p. 489–99. http://dx.doi.org/10.1016/S0167-8922(98)80104-1.
[5] Alakhramsing SS, de Rooij MB, Schipper DJ, van Drogen M. Lubrication and frictional analysis of cam–roller follower mechanisms. Proc Inst Mech Eng Part J: J Eng Tribol 2018;232(3):347–63. http://dx.doi.org/10.1177/1350650117718083.
[6] Thomson K, Dahlhaug O, Niss M, Haugset S. Technological advances in hydraulic drive trains for wind turbines. Energy Procedia 2012;24:76–82. http://dx.doi.org/10.1016/j.egypro.2012.06.089.
[7] Diepeveen NFB. On the application of fluid power transmission in offshore wind turbines (Ph.D. thesis), Delft: Delft University of Technology; 2013.
[8] Chen W, Wang X, Zhang F, Liu H, Lin Y. Review of the application of hydraulic technology in wind turbine. Wind Energy 2020;23(7):1495–522. http://dx.doi.org/10.1002/we.2506.
[9] Umaya M, Noguchi T, Uchida M, Shibata M, Kawai Y, Notomi R. Wind power generation—development status of offshore wind turbines. Mitsubishi Heavy Ind Tech Rev 2013;50(3):29–35.
[10] Nijssen J, Kempenaar A, Diepeveen N. Development of an interface between a plunger and an eccentric running track for a low-speed seawater pump. In: 11th international fluid power conference. 2018;11. IFK:pages 370–379. http://dx.doi.org/10.18154/RWTH-2018-224521, URL http://publications.rwth-aachen.de/record/724062 Artwork Size: pages 370-379 Publisher: RWTH Aachen University.
[11] Tao J, Wang H, Liao H, Yu S. Mechanical design and numerical simulation of digital-displacement radial piston pump for multi-megawatt wind turbine drivetrain. Renew Energy 2019;143:995–1009. http://dx.doi.org/10.1016/j.renene.2019.04.159.
[12] Amoroso P, van Ostayen RAJ, Perassi F. Rolling-sliding performance of radial and offset roller followers in hydraulic drivetrains for large scale applications: A comparative study. Machines 2023;11(6):604. http://dx.doi.org/10.3390/machines11060604.
[13] Amoroso P, van Ostayen RAJ, de Rooij MB. Rolling pairs with shifting contact geometry: Design, development, and validation. Proc Inst Mech Eng Part J: J Eng Tribol 2024;238(8). http://dx.doi.org/10.1177/13506501241239490.
[14] Nijssen JPA, van Ostayen RAJ. Compliant hydrostatic bearings utilizing functionally graded materials. J Tribol 2020;142(11):111801. http://dx.doi.org/10.1115/1.4047299.
[15] van Beek A, Segal A. Rubber supported hydrostatic thrust bearings with rigid bearing surfaces. Tribol Int 1997;30(1):47–52. http://dx.doi.org/10.1016/0301-679X(96)00021-7.
[16] Liang X, Yan X, Ouyang W, Wood RJK, Liu Z. Thermo-elasto-hydrodynamic analysis and optimization of rubber-supported water-lubricated thrust bearings with polymer coated pads. Tribol Int 2019;138:365–79. http://dx.doi.org/10.1016/j.triboint.2019.06.012.
[17] Dowson D, Taylor CM. Elastohydrostatic lubrication of circular plate thrust bearings. J Lubr Technol 1967;89(3):237–42. http://dx.doi.org/10.1115/1.3616957.
[18] Castelli V, Rightmire GK, Fuller DD. On the analytical and experimental investigation of a hydrostatic, axisymmetric compliant-surface thrust bearing. J Lubr Technol 1967;89(4):510–9. http://dx.doi.org/10.1115/1.3617045.
[19] van Beek A, Lepic L. Rubber supported hydrostatic thrust bearings with elastic bearing surfaces of infinite length. Wear 1996;201(1):45–50. http://dx.doi.org/10.1016/S0043-1648(96)06987-6.
[20] van Ostayen RAJ, van Beek A, Ros M. A parametric study of the hydro-support. Tribol Int 2004;37(8):617–25. http://dx.doi.org/10.1016/j.triboint.2004.01.009.
[21] Jackson RL. Self adapting mechanical step bearings for variations in load. Tribol Lett 2005;20(1):11–20. http://dx.doi.org/10.1007/s11249-005-7788-y.
[22] Nijssen JPA, van Ostayen RAJ. Passive shape shifting: A compliant design approach for full film bearings. Proc Inst Mech Eng Part C: J Mech Eng Sci 2021;235(24). http://dx.doi.org/10.1177/09544062211003616.
[23] Marinescu A, Cicone T, Fatu A. The study of a novel hydrostatic thrust bearing with a structurally elastic component: Theory and experiments. Tribol Int 2023;189:108954. http://dx.doi.org/10.1016/j.triboint.2023.108954.
[24] van Parijs V, Nijssen JP, van Ostayen RA. Whiffletree based supports for self-adjustable hydrostatic bearings. Adv Mech Eng 2021;13(12). http://dx.doi.org/10.1177/16878140211055573.
[25] Manring ND, Johnson RE, Cherukuri HP. The impact of linear deformations on stationary hydrostatic thrust bearings. J Tribol 2002;124(4):874–7. http://dx.doi.org/10.1115/1.1482118.
[26] Nijssen JPA. Compliant full film lubricated bearings: Concept design & development. (PhD Thesis), Delft: Delft University of Technology; 2022, http://dx.doi.org/10.4233/uuid:b0a6cb46-5b3d-47a5-9cbc-3db7cdd42a4a.
[27] Sonneveld DD, van Ostayen RAJ. Highly deformable hydrostatic bearings using a single closed fluid cell. Proc Inst Mech Eng Part J: J Eng Tribol 2025. http://dx.doi.org/10.1177/13506501251315977.
[28] Snieder J. Film height in soft elastohydrodynamic lubrication (Ph.D. thesis), Delft University of Technology; 2026, http://dx.doi.org/10.4233/uuid:e117b8a4-dbe7-4a31-adeb-299b625e2ae1.
[29] Karaszkiewicz A. Hydrodynamics of rubber seals for reciprocating motion. Ind Eng Chem Prod Res Dev 1985;24(2):283–9. http://dx.doi.org/10.1021/i300018a022.
[30] Kanters A, Verest J, Visscher M. On reciprocating elastomeric seals: Calculation of film thicknesses using the inverse hydrodynamic lubrication theory. Tribol Trans 1990;33(3):301–6. http://dx.doi.org/10.1080/10402009008981959.
[31] Hamrock BJ, Schmid SR, Jacobson BO. Fundamentals of fluid film lubrication, In: Mechanical engineering, second ed.. New York: Marcel Dekker; 2004, no. 169.
[32] COMSOL multiphyscis®. 2026, v. 6.2. COMSOL AB, Stockholm, Sweden. Available online: www.comsol.com [Accessed 09 February 2026].
[33] COMSOL application gallery, large deformation analysis of a beam. 2026, URL https://www.comsol.com/model/large-deformation-analysis-of-a-beam-204 [Accessed 11 February 2026].
[34] Kármán TV. Festigkeitsprobleme im maschinenbau. In: Encyklopädie der mathematischen wissenschaften, Teubner; 1910.
[35] Timoshenko S, Woinowsky-Kreiger S. Theory of Plates and Shells. second ed.. New York: McGraw-Hill Book Company; 1959.